ELSEVIER

Chemical Geology 199 (2003) 159–177

CHEMICAL GEOLOGY
INCLUDING
ISOTOPE GEOSCIENCE

www.elsevier.com/locate/chemgeo

In situ Pb geochronology of zircon with laser ablation–inductively coupled plasma–sector field mass spectrometry

Massimo Tiepolo*

C.N.R.-Istituto di Geoscienze e Georisorse, Sezione di Pavia, via Ferrata 1, I-27100 Pavia, Italy

Received 11 September 2002; accepted 28 February 2003

Abstract

The in situ Pb geochronological capabilities of a laser ablation–inductively coupled plasma–mass spectrometer (LA–ICP–MS) coupling a magnetic sector ICP–MS with a Nd:YAG laser probe working at 213 nm have been tested on three zircon populations with different age (150–294–577 Ma) and radiogenic Pb contents (0.7–10–40 ppm). The influence of scan mode and spatial resolution on age precision and accuracy has also been evaluated. All the signals necessary to independently determine the $^{206}Pb/^{238}U$, $^{207}Pb/^{235}U$, $^{207}Pb/^{206}Pb$ and $^{208}Pb/^{232}Th$ ratios have been acquired. The external standardization approach has been used to correct for laser induced U/Pb elemental fractionation, instrumental mass bias and sequential acquisition of transient signals. The efficiency of the external standardization correction has been carefully evaluated in each analytical session and residual error with a spot size of 40 μm has been estimated to be in the 0.1–1.5% range. Geologically meaningful ages can be achieved in zircons with less than 1 ppm of radiogenic Pb and with a spatial resolution down to 20 μm. With a spatial resolution of 40 μm, the E-scan mode is more efficient and offers, for zircon with about 40 ppm of radiogenic Pb, an internal precision (2σ) on the apparent age to better than 1.1% for all isotope ratios. At lower radiogenic Pb contents, internal precision decreases and, for zircons with radiogenic Pb contents lower than 1 ppm, is better than 7% and 2% on the $^{207}Pb/^{235}U$ and $^{206}Pb/^{238}U$ ages, respectively. Accuracy is strictly related to Pb* in zircon and ranges between 1% and 5%. At a 20 μm of spot size, internal precision and accuracy are approximately 1.5–2 times lower than at 40 μm.

Keywords: Pb geochronology; Laser ablation; Magnetic sector ICP–MS; Zircon; Scan modes

1. Introduction

Most in situ age determinations on zircon are currently carried out by means of ion-microprobe based techniques (e.g., SHRIMP II and Cameca ims 1270). In situ Pb geochronology provides grater spatial resolution on a single zircon grain if compared with conventional techniques such as TIMS, but at the cost of a lower precision (e.g., Williams, 1998). Ion-microprobes are however limited to few laboratories in the world due to their very high cost. In the last few years, thanks to instrumental advances (e.g., lasers with shorter wavelength, more sensitive ICP–mass spectrometers) laser ablation–inductively coupled plasma–mass spectrometry (LA–ICP–MS) has been demonstrated as a suitable technique for in situ Pb geochronology of zircons that may

* Tel.: +39-382-505882; fax: +39-382-505887.
E-mail address: tiepolo@crystal.unipv.it (M. Tiepolo).

0009-2541/03/$ - see front matter © 2003 Elsevier Science B.V. All rights reserved.
doi:10.1016/S0009-2541(03)00083-4

compare in terms of precision and accuracy with SHIRIMP II on Proterozoic zircons (Feng et al., 1993; Fryer et al., 1993; Horn et al., 2000; Li et al., 2001).

The majority of published data on Pb geochronology of zircon by means of laser ablation ICP–MS (Fryer et al., 1993; Horn et al., 2000; Li et al., 2000, 2001) have been carried out with quadrupole-based mass spectrometers whose high scan speed allows a better acquisition of the rapidly varying signals produced by laser ablation. However, these mass spectrometers are not the most suitable instruments for isotope determinations. When dealing with Pb geochronology, a series of instrumental impediments (e.g., low abundance sensitivity, not "flat top" peak shape and generally lower sensitivity) limit the spatial resolution and the minimum detectable age. Recently, multi-collector (MC) LA–ICP–MS instruments have been successfully used for Pb geochronology of zircons (Horstwood et al., 2001; Machado and Simonetti, 2001); however, their availability is still limited by the very high costs.

Single-collector double-focusing magnetic sector mass spectrometers represent a good compromise between MC–ICP–MS and quadrupoles. Despite the fact they are usually considered not suitable for LA–ICP–MS application because of the low scan speed, Latkoczy and Günther (2002) and Tiepolo et al. (in press) demonstrated that analytical results on trace element determinations, carried out with a sector-field based LA–ICP–MS, are almost comparable with those produced by quadrupoles. New generations of double-focusing magnetic sector mass spectrometers with ICP source are capable of scanning the mass spectrum both magnetically and electrostatically and, if short mass ranges are considered, they can approach scan-speed performances of quadrupoles. Advantages of magnetic sector mass spectrometers relative to quadrupoles are generally higher sensitivity, better abundance sensitivity and flat top peak shape, features required for precise isotope ratios.

This work is aimed to test the capabilities of the single-collector magnetic sector mass spectrometer coupled to a laser source working at 213 nm to provide reliable in situ Pb geochronological data on zircon. Minimum detectable age, minimum spot size as well as precision and accuracy have been evaluated using three zircon populations already dated by TIMS with different age and characterised by different radiogenic Pb contents. The best approach to standardisation and to scan mode have been also considered.

2. Instrumental configuration

2.1. Laser

The laser ablation apparatus consists of a Q-switched Nd:YAG laser source (Brilliant, Quantel) whose fundamental emission in the near-IR region (1064 nm) is converted into 266 or 213 nm by means of harmonic generators. The 266-nm configuration is described in Tiepolo et al. (in press) and derives from that developed by Jackson et al. (1992). The 213-nm laser configuration used in the present work is similar to that described in Jeffries et al. (1998). The 213-nm laser wavelength is generated by combining the first and the fourth harmonic by means of a fifth harmonic generator. Wavelength separation is obtained by means of a "Pellin-Broca" prism after which all unnecessary radiations are stopped with a dumper. Using mirrors, the 213-nm laser beam is carried into a petrographic microscope, focused above the sample and then projected onto it. The laser power is controlled by an optical attenuator consisting of a rotatable zero-order half-wave plate, a high power UV prism and a beam dump. The spot size can be varied by changing the sample position below the focus point of the laser or adding a diaphragm in the laser path. The second method is preferred when diaphragms with diameters allowing the required spot dimension are available. The maximum output energy at 213 nm is about 0.4 mJ/pulse. For the present work, the laser was operated at a frequency of 10 Hz with a fluency of about 15 J/cm^2.

Ablation is performed in an "in-house-built" ablation cell consisting of a cylinder with an internal volume of approximately 27 cm^3. He is used as the carrier gas (Eggins et al., 1998) and downstream the ablation cell it is mixed with the Ar sample gas. A cylinder with an internal volume of 125 cm^3 is placed on the gas line before the ICP torch in order

to achieve a smoothing of the signal. With this configuration, the washout time is approximately 1 min.

2.2. Mass spectrometer

The ablated material is analysed with a single-collector double focusing magnetic sector ICP–MS (Element I, ThermoFinnigan Mat). The standard torch of the Element I has been upgraded to the Capacitive Decoupling torch (CD-2) of the Element II, and the torch-positioning system has been substituted with an "in-house-built" one that ensures a more accurate movement and alignment of the torch-sample cone system.

The ICP–MS was operated at low resolution for the present work. A fine alignment (optimum RF power and gas flows) is performed before every analytical session on the NIST 610 glass reference material by maximizing the signals of ^{208}Pb and ^{232}Th, by minimizing the ThO^+/Th^+ ratio (<1%) in order to reduce the formation of polyatomic oxides, and by fitting the U/Th ratio to the reference value in order to optimise particle transport to the ICP (Guillong and Günther, 2002). At the optimum instrumental operating conditions (Table 1), sensitivity on ^{232}Th and ^{238}U at 40 μm of spot size ranges between 20,000 and 30,000 cps/ppm. Background values in counting mode are approximately 3000 cps ^{202}Hg, 300 cps ^{207}Pb and 5 cps ^{235}U.

Table 1
Instrumental details

Laser source		
Model	Brilliant, Quantel	
Type	Nd:YAG	
Wavelength	213 nm	
Repetition rate	10 Hz	
ICP-MS		
Model	Element I, ThermoFinnigan	
ICP torch	Capacitive Decoupling	CD-2
RF power		900 W
Gas flow	cooling gas	13.5 l/min
	auxiliary gas	1.5 l/min
	carrier gas I (Ar)	1.2 l/min
	carrier gas II (He)	1.2 l/min
Dead time value of the detector		25 ns

3. Analytical method

3.1. Data acquisition

In order to completely apply the U–Th–Pb systematics, the signals of masses ^{202}Hg, ^{204}(Pb + Hg), ^{206}Pb, ^{207}Pb, ^{208}Pb, ^{232}Th, ^{235}U and ^{238}U are acquired. The measurement of ^{202}Hg signal allows correction for the isobaric interference of ^{204}Hg on ^{204}Pb and thus estimation of common Pb in zircon. Detection of very small amounts of common Pb is however currently hampered by the presence of a relatively high amount of Hg in the gas blank that causes a relatively high background level on 204 mass. We preferred to acquire the signal of ^{235}U, rather than to recalculate it on the basis of the natural $^{238}U/^{235}U$ ratio (e.g., Horn et al., 2000) to obtain two independent and not correlated determinations, although at cost of a slightly longer scan time.

The element double-focusing mass spectrometer allows one to scan the mass spectrum both magnetically and electrostatically. In magnetic scan (B-scan), ion selection is obtained by varying the magnetic field and the electrostatic sector has only function to recover on the right path the ions with the same mass but different energy. The Element I is not equipped with the fast-scanning option thus the B-scan mode is relatively slow and a settling time of about 1 ms/a.m.u. is required. In electrostatic scan mode (E-scan), ion selection is operated at a constant value of the magnetic field by decreasing the ion accelerating voltage. E-scan mode can cover only a limited mass spectrum that does not exceed 30% of the current "magnet mass" (the mass set by the magnet), but it is significantly faster than B-scan mode because independently of the mass jump only 1 ms of settling time is required. The gain in scan speed achieved in E-scan mode is however counterbalanced by the loss in sensitivity (up to 40%), which is proportional to the difference from the nominal magnet mass (Tiepolo et al., in press) and related to the decrease in ion transmission efficiency as the accelerating voltage is far from that used for the instrument alignment.

The Δm (202–238) is well within the 30% mass range allowed by the E-scan mode because the ^{238}U mass is about 16% heavier than ^{202}Hg. The selected mass spectrum can be thus acquired both in magnetic and electrostatic mode. For this reason, we have compiled two acquisition lists (Table 2) in which all

Table 2
Acquisition parameters

Element	Mass	Settling time (ms)	Sample time (ms)	Samples per peak	Mass window[a] (%)
B-scan mode					
Hg	202	40	1.5	12	120
Pb	204	6	1.5	12	120
Pb	206	5	3.5/1.5	6/12	120
Pb	207	2	1.5	12	120
Pb	208	2	1.5	12	120
Th	232	25	3.5	6	120
U	235	6	1.5	12	120
U	238	6	3.5	6	120
E-scan mode					
Hg	202	1	1.5	12	120
Pb	204	1	1.5	12	120
Pb	206	1	3.5/1.5	6/12	120
Pb	207	1	1.5	12	120
Pb	208	1	1.5	12	120
Th	232	1	3.5	6	120
U	235	1	1.5	12	120
U	238	1	3.5	6	120

Double values for ^{206}Pb correspond to its acquisition in analog and counting mode, respectively.
[a] Mass window is the scanning range of the instrument around the peak.

masses are acquired in pure B-scan and E-scan modes. The combination of the two scan modes, contrarily to the trace element determination (Tiepolo et al., in press), has not been considered because of the small mass range acquired.

The acquisition list in B-scan mode is that described in Tiepolo et al. (in press). Settling times are < 6 ms for all masses with the exception of the fly-back from ^{238}U to ^{202}Hg (40 ms) and the mass jump from ^{208}Pb to ^{232}Th (25 ms). ^{238}U and ^{232}Th generally show high concentrations in zircon, thus they were detected in analog mode. Because ^{206}Pb can exceed in old and U-rich zircons the limits of the counting mode, its acquisition-mode is evaluated before every analytical session. However, the same detector mode is used on both external standards (see Section 3.2) and unknowns to overcome problems of cross calibration. The total scan-time in B-scan mode is approximately 290 ms and the acquisition efficiency (the ratio between counting time and total scan time) of about 63%. The acquisition list in E-scan mode closely resembles that in B-scan with the exception of magnet settling times that were set to 1 ms for all masses. This allowed nearly a two-time shorter scan time (about 140 ms) and an acquisition efficiency of about 94%. Noticeably, quadrupole based ICP–MS (e.g., Elan 6000, Horn personal communication) is still about twice as fast as the E-scan mode of the Element.

Single analyses consisted of 1 min of background and 1 min of ablation signal acquisition. The two acquisition lists reported above allow approximately 410 sweeps and a mean integrated acquisition time of about 4 s in B-scan and 820 sweeps and a mean integrated acquisition time of about 7 s in E-scan mode.

3.2. Standardisation

In LA–ICP–MS analysis, measured isotope ratios differ from the original values of the sample for a series of fractionation effects that are the instrumental mass discrimination (mass bias), the laser induced elemental fractionation and an effect related to the sequential acquisition of transient signals (Jackson et al., 2001). The age reliability strongly depends on the efficiency of the correction of these effects.

The major impediment during Pb geochronology by LA–ICP–MS is represented by the elemental fractionation induced by ablation, transport and excitation processes (Longerich et al., 1996b; Jackson, 2001; Günther and Hattendorf, 2001), which alters of several percent the original Pb/U ratios (Fryer et al., 1993; Longerich et al., 1996b; Hirata, 1997; Horn et al., 2000).

In the last years, several approaches have been proposed for the reduction and the correction of U/Pb laser induced elemental fractionation. Among them, there is the "cooling-jet cell" (Jackson et al., 1996), the active focusing (Hirata and Nesbitt, 1995), the adoption of highly homogeneous and stable laser sources with short wavelength allowing a mathematical correction (e.g., 193 nm; Horn et al., 2000), the rastering of the sample surface (e.g., Li et al., 2001; Horstwood et al., 2001), the adoption of a matrix matched external standard (Ketchum et al., 2001) or more sophisticated approaches such as the filtering technique (Jackson and Günther, 2002) or the chemically assisted ablation (Hirata, 2002). Tiepolo et al. (in press) adopted the matrix-matched external standardisation with the 266-nm laser configuration of the same LA–ICP–MS instrument used in this work and demonstrated that it

is suitable for the U/Pb fractionation correction if the same integration intervals are considered on standard and unknown zircons. The choice of the matrix matched external standard was mainly due to the day to day instability of the Nd:YAG laser that does not allow a mathematical approach to the correction of U/Pb fractionation as that proposed by Horn et al. (2000). The "rastering" technique, for the strong limitation on spatial resolution, which looses crucial geological information especially in zircon where inherited components are present, it has not been considered. The adoption of the matrix matched external standard allowed us to correct also for instrumental mass discrimination and for the effects related to sequential acquisition of transient signals.

We have adopted the analytical protocol of the data-reduction software package "LamTrace" (developed by S. Jackson initially at Memorial University of Newfoundland and later at Macquarie University, Sydney) that includes two blocks of four standards, one at the beginning and one at the end of the analytical run. The analysis of a reference zircon was also performed among the 12 unknown samples.

3.3. Signal acquisition and data reduction

The signals acquisition as a function of time allows a first on-line inspection of the presence of zircon heterogeneity. Data reduction was performed by the software package LamTrace and the measured $^{207}Pb/^{235}U$ ratio was considered. Time resolved analyses were carefully inspected in order to recognise perturbations in the isotope ratios. Particular attention was placed to the presence of detectable common Pb by monitoring the signal of ^{204}Pb and of eventually inherited components. Accordingly, the most reliable integration intervals of background and signal for each zircon sample were selected. Noticeably, if different grains within the same analytical run require different integration intervals, thus standards were recalculated accordingly for each different sample. Among the eight standard measurements performed during each session, only those in agreement with TIMS were considered.

Concordant ages were calculated from $^{206}Pb/^{238}U$ and $^{207}Pb/^{235}U$ ratios using the ISOPLOT software (Ludwig, 2000).

4. Samples

Zircon samples considered in this work are two standard zircons and three zircons already dated by TIMS with variable age, U and radiogenic Pb (Pb*) contents (Table 3). With the exception of standard zircons, all samples have been characterized with cathodoluminescence (model CITL Mk3) at the C.N.R.-Istituto di Geoscienze e Georisorse, Sezione di Pavia.

4.1. Standard zircons 91500 and 02123

Zircon 91500 is described in Wiedenbeck et al. (1995). This zircon has 81.2 ppm U, 28.8 ppm Th and 14.8 ppm Pb*. U and Pb have a homogeneous distribution and there is no evidence of any inherited xenocrystic component. U–Pb data show a significant degree of discordance. The mean $^{206}Pb/^{238}U$ and $^{207}Pb/^{206}Pb$ apparent ages are 1062.4 ± 0.4 and 1065.4 ± 0.3 Ma, respectively. The only two measurements of $^{208}Pb/^{232}Th$ yield an apparent age of 1058 ± 2.8 Ma. Zircon 02123 is a pegmatitic gem zircon from Norway (Ketchum et al., 2001). U and

Table 3
Selected samples

Sample	U (ppm)	Pb (ppm)	Apparent ages (Ma)			Preferred age (Ma)	Reference
			$^{207}Pb/^{206}Pb$	$^{206}Pb/^{238}U$	$^{207}Pb/^{235}U$		
91500 (standard)	81.2	14.8	1065.4	1062.4	–	–	Widenbeck et al., 1995
2123 (standard)	145–185	7.2–9.2	295	295	295	295 ± 1	Ketchum et al., 2001
GRM	~ 400	~ 40	481	499	586	577 ± 8	Paquette et al., 1994
NYP	–	~ 10	294 ± 1	–	–	–	J.L. Paquette, personal communication
AMV	~ 42	~ 0.7	149	147	147	150 ± 2	Seyler et al., 1998

Pb*: radiogenic Pb.

Pb* contents range from 145 to 185 and from 7.2 to 9.2 ppm, respectively. TIMS data on this zircon yield a concordant age of 295 ± 1 Ma.

The relatively higher Pb* content of zircon 91500 relative to 02123 allowed a better signal on the critical ^{207}Pb mass and thus a better internal precision on the $^{207}Pb/^{235}U$ ratio. For this reason, zircon 91500 has been adopted as external standard.

Three fragments of zircon 91500 of about 5 × 5 mm and one fragment of zircon 02123 of about 10 × 10 mm were mounted in two distinct epoxy resin discs and then polished down to 0.25 μm. Before every analytical session, standard samples were repolished and washed in ultrasound bath for 30 min with ethylic alcohol in order to remove any residual of particulate deposition from previous ablations. Ethylic alcohol is also used to clean the side wall and the floor of the ablation cell.

4.2. Zircons GRM, NYP and AMV

Zircons GRM are from a granulite domain in SE Madagascar (sample A1010; Paquette et al., 1994). With our instrument, these zircons show a very weak cathodo-luminescence and do not allow the production of printable images. According to Paquette et al. (1994), under CL trace elements do not show any zoned distribution but rather rounded domains. GRM zircons have approximately U and Pb* contents of 400 and 40 ppm, respectively. The three grain fractions analysed by Paquette et al. (1994) yielded discordant ages. The $^{206}Pb/^{238}U$ and $^{207}Pb/^{235}U$ apparent ages range from 481 to 564 and from 499 to 567 Ma, respectively, and define a discordant array with an upper intercept at 577 ± 8 Ma. The $^{207}Pb/^{206}Pb$ apparent age ranges between 586 and 579 Ma. For the present work, about 30 grains of GRM zircons with dimensions of about 200–300 μm have been embedded in epoxy resin then polished down to 0.25 μm. On zircons GRM three different analytical runs were carried out. Two runs at 40 μm of spot size considering the two different acquisition lists (in B-scan and E-scan mode) reported above and one run at 20 μm of spot size using the B-scan mode.

Zircons NYP are from a norite of Pyrenees (J.-L. Paquette, personal communication). About 30 grains with dimensions of about 40–80 μm were embedded in epoxy resin, polished and then analysed by CL. These zircons (Fig. 1) reveal the presence of a small optically brighter rim different from the dark core, but no inherited cores were observed in analysed samples. All U–Th–Pb determinations have been carried out on the dark cores. The average Pb* content of these zircon is about 10 ppm and the $^{207}Pb/^{206}Pb$ apparent age determined by TIMS is

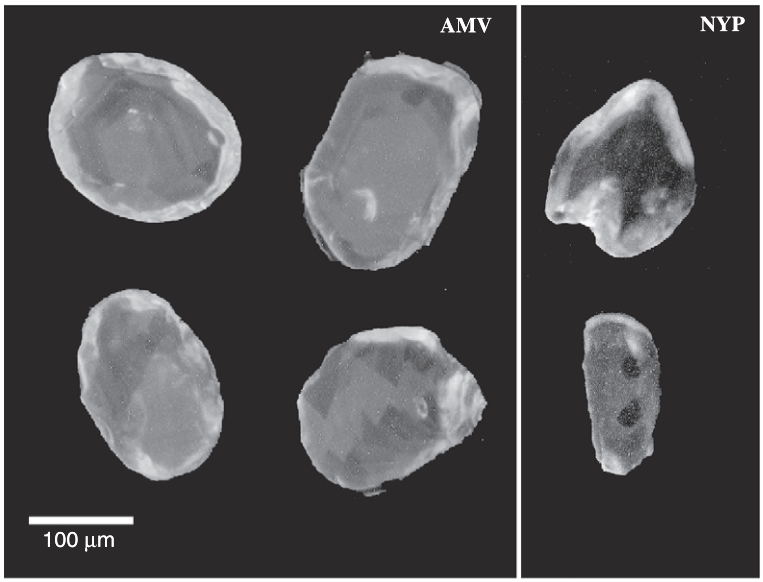

Fig. 1. CL images of representative zircons from samples AMV and NYP.

Table 4
Isotope ratios after external standard correction and U/Pb fractionation values for selected samples

Sample	Spot size	Scan mode	α_{smp} (s^{-1})	$^{206}Pb/^{238}U$	1σ (%)	$^{207}Pb/^{235}U$	1σ (%)	$^{207}Pb/^{206}Pb$	1σ (%)	$^{208}Pb/^{232}Th$	1σ (%)
GRM	40	B-scan	0.12%	0.094	0.54	0.749	1.16	0.058	1.04	0.027	0.66
GRM	40	B-scan	0.15%	0.092	0.64	0.733	1.30	0.058	0.96	0.028	0.68
GRM	40	B-scan	0.15%	0.092	0.53	0.750	1.03	0.059	0.98	0.027	0.68
GRM	40	B-scan	0.13%	0.092	0.48	0.759	1.13	0.060	1.16	0.028	0.73
GRM	40	B-scan	0.14%	0.095	0.56	0.769	1.14	0.059	1.07	0.030	0.86
GRM	40	B-scan	0.13%	0.093	0.54	0.765	1.11	0.060	1.15	0.028	0.73
GRM	40	B-scan	0.10%	0.093	0.51	0.749	1.00	0.059	0.96	0.028	0.66
GRM	40	B-scan	0.16%	0.094	0.60	0.760	1.08	0.058	0.95	0.029	0.67
GRM	40	B-scan	0.12%	0.093	0.53	0.762	0.99	0.060	0.98	0.028	0.58
GRM	40	B-scan	0.11%	0.093	0.55	0.757	1.14	0.059	1.11	0.028	0.65
GRM	40	B-scan	0.09%	0.095	0.50	0.787	1.23	0.060	1.27	0.029	0.80
GRM	40	E-scan	0.07%	0.090	0.48	0.748	0.74	0.060	0.70	0.028	0.51
GRM	40	E-scan	0.07%	0.095	0.49	0.770	0.71	0.059	0.65	0.030	0.46
GRM	40	E-scan	0.04%	0.092	0.47	0.760	0.71	0.060	0.66	0.026	0.49
GRM	40	E-scan	0.08%	0.091	0.43	0.762	0.81	0.061	0.85	0.026	0.43
GRM	40	E-scan	0.06%	0.099	0.46	0.795	0.71	0.058	0.67	0.031	0.50
GRM	40	E-scan	0.05%	0.095	0.46	0.751	0.71	0.057	0.71	0.029	0.47
GRM	40	E-scan	0.04%	0.091	0.46	0.753	0.81	0.060	0.78	0.027	0.49
GRM	40	E-scan	0.07%	0.093	0.43	0.744	0.83	0.058	0.75	0.027	0.46
GRM	40	E-scan	0.07%	0.093	0.43	0.746	0.77	0.058	0.69	0.027	0.44
GRM	40	E-scan	0.05%	0.091	0.43	0.747	0.94	0.059	0.95	0.027	0.54
GRM	40	E-scan	0.06%	0.092	0.44	0.752	0.73	0.059	0.71	0.027	0.41
GRM	20	B-scan	0.32%	0.093	0.67	0.736	1.37	0.058	1.44	0.027	1.07
GRM	20	B-scan	0.40%	0.085	1.02	0.694	2.07	0.059	1.98	0.026	1.42
GRM	20	B-scan	0.27%	0.096	0.90	0.768	2.29	0.058	1.73	0.029	1.27
GRM	20	B-scan	0.37%	0.098	0.84	0.774	1.77	0.058	1.67	0.029	1.12
GRM	20	B-scan	0.31%	0.095	0.68	0.772	1.33	0.059	1.32	0.029	0.85
GRM	20	B-scan	0.29%	0.092	0.80	0.743	1.53	0.059	1.52	0.027	0.97
GRM	20	B-scan	0.35%	0.095	0.83	0.777	1.77	0.059	1.69	0.028	1.26
GRM	20	B-scan	0.31%	0.096	0.69	0.774	1.64	0.059	1.62	0.028	1.00
GRM	20	B-scan	0.32%	0.097	0.69	0.783	1.61	0.059	1.65	0.028	1.04
GRM	20	B-scan	0.38%	0.098	0.84	0.805	1.54	0.060	1.30	0.028	1.17
GRM	20	B-scan	0.21%	0.094	0.97	0.778	1.49	0.060	1.50	0.030	0.93
NYP	20	E-scan	0.16%	0.046	1.57	0.395	6.8	–	–	0.012	3.7
NYP	20	E-scan	0.32%	0.048	1.76	0.403	9.5	–	–	0.014	4.2
NYP	20	E-scan	0.35%	0.046	1.94	0.391	9.7	–	–	0.015	5.4
NYP	20	E-scan	0.29%	0.044	1.86	0.297	7.6	–	–	0.013	4.8
NYP	20	E-scan	0.16%	0.046	1.34	0.366	6.2	–	–	0.014	4.0
NYP	20	E-scan	0.35%	0.052	2.34	0.532	11.1	–	–	0.017	4.4
NYP	20	E-scan	0.21%	0.046	1.49	0.342	5.2	–	–	0.014	2.3
NYP	20	E-scan	0.17%	0.044	1.88	0.320	7.6	–	–	0.013	3.8
NYP	20	E-scan	0.37%	0.046	2.05	0.318	9.3	–	–	0.011	18.3
NYP	20	E-scan	0.26%	0.048	1.78	0.424	7.9	–	–	0.016	3.6
NYP	20	E-scan	0.28%	0.047	1.85	0.690	5.8	–	–	0.023	2.9
NYP	20	B-scan	0.31%	0.048	1.24	0.372	4.85	–	–	0.012	5.49
NYP	20	B-scan	0.31%	0.046	1.30	0.469	4.73	–	–	0.016	3.06
NYP	20	B-scan	0.33%	0.050	1.20	0.370	4.96	–	–	0.013	2.56
NYP	20	B-scan	0.26%	0.050	1.14	0.360	4.30	–	–	0.014	2.41
NYP	20	B-scan	0.35%	0.047	1.04	0.364	3.90	–	–	0.013	1.88
NYP	20	B-scan	0.28%	0.047	1.04	0.346	4.74	–	–	0.013	2.12
NYP	20	B-scan	0.29%	0.046	0.95	0.325	3.89	–	–	0.012	1.75

(continued on next page)

Table 4 (*continued*)

Sample	Spot size	Scan mode	α_{smp} (s^{-1})	$^{206}Pb/^{238}U$	1σ (%)	$^{207}Pb/^{235}U$	1σ (%)	$^{207}Pb/^{206}Pb$	1σ (%)	$^{208}Pb/^{232}Th$	1σ (%)
NYP	20	B-scan	0.30%	0.047	1.15	0.342	4.67	–	–	0.013	3.08
NYP	20	B-scan	0.31%	0.046	1.16	0.329	4.77	–	–	0.013	2.46
NYP	20	B-scan	0.26%	0.046	1.04	0.321	4.26	–	–	0.013	2.09
NYP	20	B-scan	0.28%	0.047	0.99	0.345	3.72	–	–	0.012	2.35
AMV	40	B-scan	0.12%	0.023	1.50	0.168	5.8	–	–	0.007	4.9
AMV	40	B-scan	0.10%	0.022	1.69	0.162	8.5	–	–	0.008	5.2
AMV	40	B-scan	0.07%	0.022	1.84	0.191	8.3	–	–	0.007	8.3
AMV	40	B-scan	0.11%	0.022	1.85	0.182	8.5	–	–	0.009	6.4
AMV	40	B-scan	0.05%	0.022	1.64	0.156	6.6	–	–	0.008	5.0
AMV	40	B-scan	0.07%	0.021	1.74	0.150	8.3	–	–	0.007	6.6
AMV	40	B-scan	0.14%	0.021	1.58	0.187	10.5	–	–	0.008	6.8
AMV	40	B-scan	0.04%	0.022	2.24	0.167	6.7	–	–	0.008	5.5
AMV	40	B-scan	0.04%	0.022	1.94	0.164	8.0	–	–	0.007	5.1
AMV	40	B-scan	0.28%	0.021	2.80	0.124	19.8	–	–	0.008	11.3
AMV	40	B-scan	0.16%	0.022	2.11	0.153	11.4	–	–	0.007	5.2
AMV	40	E-scan	0.06%	0.022	0.89	0.153	3.2	–	–	0.007	2.2
AMV	40	E-scan	0.08%	0.022	0.95	0.174	4.0	–	–	0.007	2.9
AMV	40	E-scan	0.05%	0.021	0.90	0.166	4.9	–	–	0.007	3.0
AMV	40	E-scan	0.05%	0.022	0.90	0.167	3.9	–	–	0.008	2.6
AMV	40	E-scan	0.04%	0.023	0.83	0.181	2.9	–	–	0.009	1.7
AMV	40	E-scan	zoned	0.027	1.60	0.615	5.9	–	–	0.032	4.7
AMV	40	E-scan	0.15%	0.024	0.83	0.167	3.3	–	–	0.009	2.4
AMV	40	E-scan	0.09%	0.023	1.00	0.175	4.0	–	–	0.009	2.7
AMV	40	E-scan	0.09%	0.024	0.97	0.176	4.2	–	–	0.008	2.6
AMV	40	E-scan	0.08%	0.023	1.03	0.182	4.4			0.009	3.0
AMV	40	E-scan	0.06%	0.023	1.01	0.178	3.4	–	–	0.010	3.3
02123/AMV	40	B-scan	0.11%	0.046	0.790	0.342	2.680	–	–	0.015	1.1
02123/AMV	40	E-scan	0.06%	0.047	1.547	0.352	3.008	–	–	0.014	0.7
02123/NYP	20	E-scan	0.27%	0.046	1.470	0.353	4.420	–	–	0.014	2.4
02123/NYP	20	B-scan	0.27%	0.049	0.910	0.368	3.320	–	–	0.013	2.1
02123/GRM	40	B-scan	0.13%	0.049	0.770	0.364	2.120	–	–	0.015	1.1
02123/GRM	20	B-scan	0.28%	0.045	1.310	0.338	4.690	–	–	0.015	2.6
02123/GRM	40	E-scan	0.07%	0.050	2.040	0.397	4.420	–	–	0.015	0.8

294 ± 1 Ma (J.-L. Paquette, personal communication). Because of the limited grain dimensions, zircon NYP was analysed only at 20 μm of spot size using both B-scan and E-scan modes.

Zircons AMV are from felsic rocks (T90-6 granulite) from the Tinaquillo massif (Venezuela) and have been studied by Seyler et al. (1998). Thirty-two grains of AMV zircons, ranging in dimension from 100 to 200 μm, were mounted in epoxy resin and then analysed by CL. AMV zircons are highly cathodo-luminescent according to the very low U (about 40 ppm) contents. Pb* contents are lower than 1 ppm. They are colourless and with no evidence of zoning (Fig. 1). The four grain-size fractions analysed by Seyler et al. (1998) by TIMS gave discordant ages. The $^{206}Pb/^{238}U$ and $^{207}Pb/^{235}U$ apparent ages range from 141 to 147 and from 127 to 147 Ma, respectively. They define a chord intersecting the concordia curve at 150 ± 2 Ma. The $^{207}Pb/^{206}Pb$ apparent age is 149 Ma. Due to the very low contents of Pb*, zircon AMV was analysed only at 40 μm of spot size in two different analytical runs using B-scan and E-scan acquisition lists.

5. Results

5.1. Evaluation of U/Pb fractionation at 213 nm

The U/Pb laser induced elemental fractionation was evaluated on a relative basis according to Tiepolo

et al. (in press) by considering the slope (α) of the regression line of the $^{206}Pb/^{238}U$ ratio vs. time. This slope was calculated in an interval of 60 s, normalized to the average value and multiplied by 100 in order to give the relative percent variation of the $^{206}Pb/^{238}U$ ratio per second.

In Table 4, the average fractionation slope values for the different samples and at the different conditions are reported. The average $^{206}Pb/^{238}U$ fractionation per second at 40 and 20 μm of spot size in B-scan mode ranges between 0.10% and 0.13% and 0.24% and 0.32%, respectively. At 213 nm of laser wavelength, an increase of two times of elemental fractionation from 40 to 20 μm of spot size has thus been observed. This is in agreement with the strong control exerted by spot geometry on elemental fractionation (Mank and Mason, 1999; Horn et al., 2000;). U/Pb fractionation values in E-scan mode are statistically equivalent ($\pm 2\sigma$) to those in B-scan with the exception of those determined on sample GRM. Since U/Pb fractionation values in B-scan and E-scan are almost comparable in the other two samples, the observed difference is most likely related to a day to day variation of laser homogeneity rather than a direct influence of the acquisition mode on the evaluation of elemental fractionation.

In order to evaluate the influence of laser wavelength on U/Pb fractionation, the results obtained at 213 nm on zircon 91500 in this work have been compared with those from Tiepolo et al. (in press) determined on the same sample and with the same instrumental conditions but working at 266 nm of laser wavelength. As shown in Fig. 2, where U/Pb fractionation per second as a function of spot size for zircon 91500 is reported, data at 213 nm are statistically equivalent to those obtained at 266 nm. This seems to suggests that the 213-nm laser wavelength does not produce any significant gain in the reduction of the elemental fractionation; for better results, shorter radiations (e.g., 193 nm; Günther and Heinrich, 1999) or better homogenized 266 nm laser beams (Guillong et al., 2002) are therefore required. However, results from the present work seem to indicate a slightly better reproducibility of elemental fractionation with a 213-nm than with 266-nm laser wavelength. This holds expecially at 40 μm of spot size, where U/Pb reproducibility is approximately two times higher than at 266 nm and probably reflects more reproducible conditions of laser energy distribution.

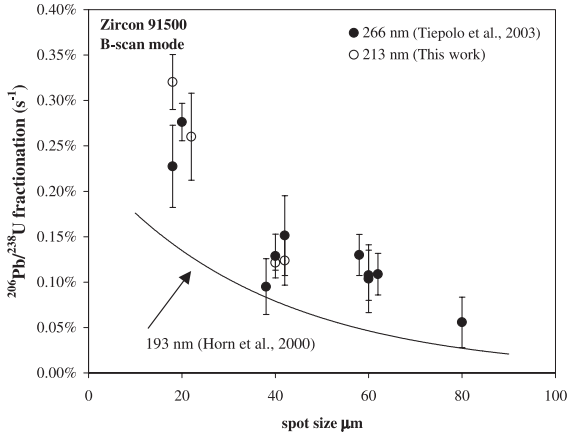

Fig. 2. Comparison between $^{206}Pb/^{238}U$ laser-induced elemental fractionation at 266 and 213 nm of laser radiation.

5.2. Evaluation of the external standardization efficiency

Residual errors (R) stemming from U/Pb elemental fractionation after external standard correction have been calculated according to the following equation:

$$R = \alpha_{std} - \alpha_{smp}$$

where α_{std} is the U/Pb fractionation per second averaged on all standard measurements and α_{smp} is the U/Pb fractionation per second of each unknown sample.

In the run carried out at 40 μm of spot size in B-scan mode on zircons GRM (Fig. 3a), maximum and minimum residual errors on $^{206}Pb/^{238}U$ stemming from elemental fractionation after external standard correction are approximately 0.035% and 0.005% per second. The mean integration time for these zircons is approximately 40 s and the average isotope ratio, approximating a steady increase of the U/Pb fractionation, corresponds to half of the integration time. The maximum and the minimum residual errors on the final ratio are thus obtained by multiplying the above values for half of the integration time and they are about 0.7% and 0.1%, respectively. According to this procedure, residual errors on the final U/Pb ratio for the runs on GRM

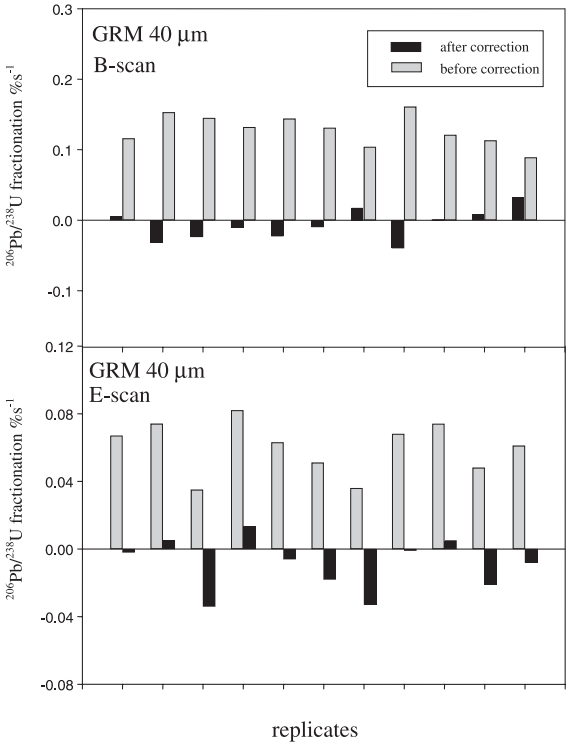

Fig. 3. $^{206}Pb/^{238}U$ laser-induced elemental fractionation in B-scan and E-scan mode on sample GRM before and after correction for the external standard.

zircons carried out at 40 µm of spot size in E-scan mode (Fig. 3b) and at 20 µm of spot size in B-scan mode are about 0.04–0.07% and 0.4–2.2%, respectively. In the two runs carried out on zircons NYP, the final U/Pb ratio after correction and integration is affected by a residual errors of 0.2–1.3% in B-scan and 1.0–3.2% in E-scan mode. On AMV zircons (40 µm of spot size), the maximum error on the final U/Pb ratio is about 1.5% in E-scan mode and lower than 1.6% in B-scan mode. In both cases, minimum error is lower than 1%.

Data indicate that the adoption of a matrix matched external standard do not allow the complete correction of the U/Pb laser induced elemental fractionation but, in most cases, gives residual errors lower than 1.5% on the final U/Pb ratio. Moreover, the external standard correction seems more efficient at larger spot size. The residual error variability, occasionally observed, is most likely

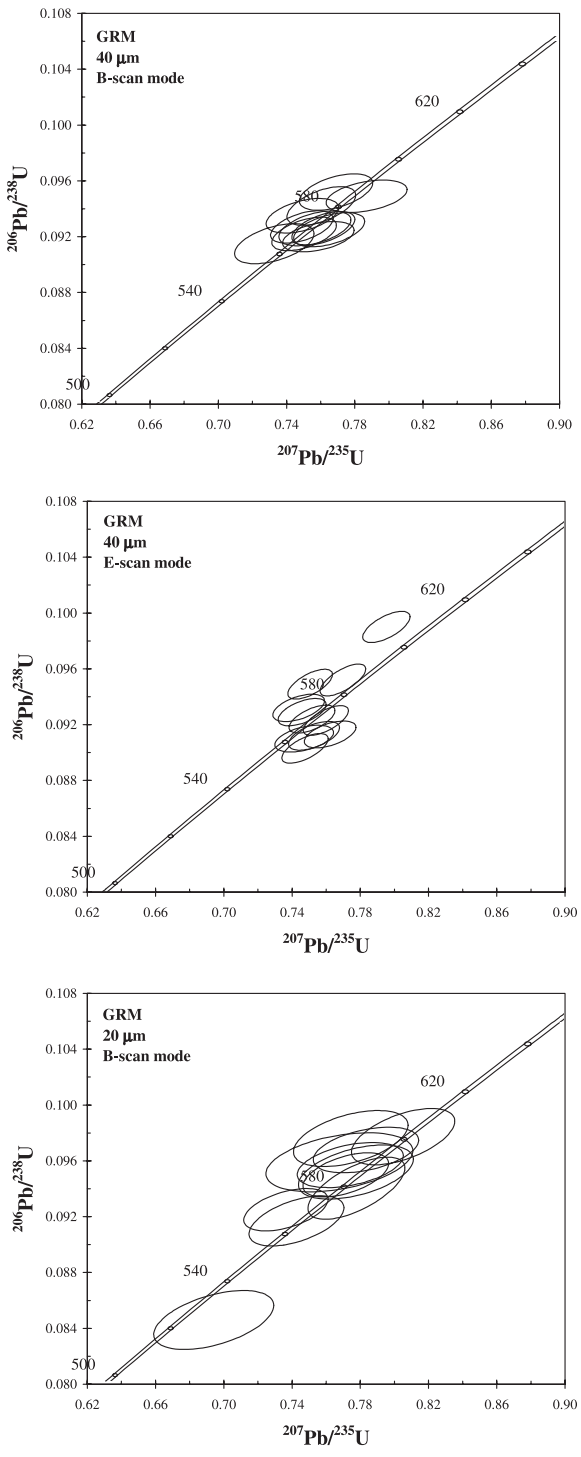

Fig. 4. Concordia diagrams for sample GRM.

Table 5
LA-ICP-MS age results

Sample	Spot diameter	Scan mode	$^{206}Pb/^{238}U$		$^{207}Pb/^{235}U$		Concordant age	± 2 S.D.	$^{207}Pb/^{206}Pb$		$^{208}Pb/^{232}Th$	
			Age (Ma)	± 2 S.D.	Age (Ma)	± 2 S.D.			Age (Ma)	± 2 S.D.	Age (Ma)	± 2 S.D.
GRM	40	B-scan	576	6	568	10	575	5.8	526	44	541	7
GRM	40	B-scan	564	7	558	11	564	6.8	534	42	550	7
GRM	40	B-scan	569	6	568	9	568	5.8	562	42	545	7
GRM	40	B-scan	568	5	573	10	568	5.2	598	50	552	8
GRM	40	B-scan	586	6	579	10	585	6.2	548	46	602	10
GRM	40	B-scan	570	6	577	10	571	5.8	614	50	565	8
GRM	40	B-scan	571	6	568	9	571	5.6	558	42	556	7
GRM	40	B-scan	580	7	574	9	579	6.6	544	42	585	8
GRM	40	B-scan	571	6	575	9	571	5.8	586	44	561	6
GRM	40	B-scan	571	6	572	10	571	6.0	576	50	562	7
GRM	40	B-scan	584	6	589	11	584	5.6	608	56	570	9
Weighted average			573	4.6	573	4.8	573	4.4	565	14.0	558	9.0
GRM	40	E-scan	557	5	567	6	–	–	604	30	553	6
GRM	40	E-scan	586	6	580	6	–	–	552	30	595	5
GRM	40	E-scan	569	5	574	6	–	–	590	28	526	5
GRM	40	E-scan	563	5	575	7	–	–	620	36	519	4
GRM	40	E-scan	608	5	594	6	–	–	538	30	608	6
GRM	40	E-scan	584	5	569	6	–	–	504	32	573	5
GRM	40	E-scan	562	5	570	7	–	–	598	34	541	5
GRM	40	E-scan	574	5	565	7	–	–	524	32	544	5
GRM	40	E-scan	572	5	566	7	–	–	538	30	541	5
GRM	40	E-scan	562	5	567	8	561	4.6	584	40	531	6
GRM	40	E-scan	570	5	569	6	570	4.7	566	30	541	4
Weighted average			573	9.8	573	5.9	–	–	564	24	549	18
GRM	20	B-scan	570	7	560	12	569	7	520	64	537	11
GRM	20	B-scan	524	10	535	17	524	10	584	86	511	14
GRM	20	B-scan	591	10	578	20	590	10	516	76	584	15
GRM	20	B-scan	600	10	582	16	–	–	512	74	581	13
GRM	20	B-scan	585	8	581	12	584	8	562	58	574	10
GRM	20	B-scan	565	9	564	13	565	9	558	66	532	10
GRM	20	B-scan	586	9	584	16	586	9	574	74	562	14
GRM	20	B-scan	589	8	582	15	589	8	554	70	555	11
GRM	20	B-scan	596	8	587	14	595	8	556	72	559	11
GRM	20	B-scan	601	10	600	14	600	10	594	56	566	13
GRM	20	B-scan	579	11	584	13	580	10	602	64	599	11
Weighted average			585	9	579	9	583	9	560	20.0	560	17.0
NYP	20	E-scan	291	9	338	39	–	–	–	–	248	18
NYP	20	E-scan	299	10	344	55	299	10	–	–	284	24
NYP	20	E-scan	289	11	335	56	289	11	–	–	304	32
NYP	20	E-scan	276	10	264	35	276	10	–	–	262	25
NYP	20	E-scan	290	8	316	34	290	7.6	–	–	282	22
NYP	20	E-scan	~~324~~	~~15~~	~~433~~	~~78~~	–	–	–	–	~~341~~	~~30~~
NYP	20	E-scan	288	8	299	27	287	8.4			283	13
NYP	20	E-scan	278	10	282	37	278	10			257	20
NYP	20	E-scan	292	12	280	46	292	12	–	–	222	81
NYP	20	E-scan	305	11	359	47	–	–	–	–	316	23
NYP	20	E-scan	~~294~~	~~11~~	~~533~~	~~48~~	–	–	–	–	~~460~~	~~26~~
Weighted average			289	6.5	306	24	287	7			276	17
NYP	20	B-scan	303	7	321	27	303	7.4	–	–	245	27
NYP	20	B-scan	289	7	390	31	–	–	–	–	326	20

(continued on next page)

Table 5 (*continued*)

Sample	Spot diameter	Scan mode	$^{206}Pb/^{238}U$		$^{207}Pb/^{235}U$		Concordant age	± 2 S.D.	$^{207}Pb/^{206}Pb$		$^{208}Pb/^{232}Th$	
			Age (Ma)	± 2 S.D.	Age (Ma)	± 2 S.D.			Age (Ma)	± 2 S.D.	Age (Ma)	± 2 S.D.
NYP	20	B-scan	312	7	320	27	312	7.4	–	–	269	14
NYP	20	B-scan	317	7	312	23	316	7	–	–	279	13
NYP	20	B-scan	299	6	315	21	299	6	–	–	254	9
NYP	20	B-scan	297	6	301	25	297	6	–	–	252	11
NYP	20	B-scan	287	5	285	19	287	5.4	–	–	250	9
NYP	20	B-scan	293	7	299	24	293	6.6	–	–	254	16
NYP	20	B-scan	287	7	289	24	287	6.6	–	–	259	13
NYP	20	B-scan	292	6	282	21	292	6	–	–	266	11
NYP	20	B-scan	296	6	301	19	296	6	–	–	244	11
Weighted average			296	6.3	300	7.1	297	6.6			256	7.4
AMV	40	B-scan	143	4	158	17	143	4.2	–	–	139	14
AMV	40	B-scan	139	5	152	24	139	4.6	–	–	153	16
AMV	40	B-scan	138	5	177	27	–	–	–	–	147	24
AMV	40	B-scan	140	5	170	27	–	–	–	–	180	23
AMV	40	B-scan	142	5	147	18	142	4.6	–	–	157	16
AMV	40	B-scan	135	5	142	22	135	4.6	–	–	136	18
AMV	40	B-scan	136	4	174	34	–	–	–	–	162	22
AMV	40	B-scan	142	6	157	19	142	6.2	–	–	161	18
AMV	40	B-scan	142	5	154	23	142	5.4	–	–	150	15
AMV	40	B-scan	136	8	119	44	136	7.6	–	–	151	34
AMV	40	B-scan	142	6	144	31	142	6	–	–	135	14
Weighted average			140	1.5	155	7	140	1.8			149	8.4
AMV	40	E-scan	138	2	145	9	138	2.4	–	–	149	7
AMV	40	E-scan	141	3	163	12	–	–	–	–	147	8
AMV	40	E-scan	136	2	156	14	–	–	–	–	150	9
AMV	40	E-scan	137	2	157	11	–	–	–	–	151	8
AMV	40	E-scan	145	2	169	9	–	–	–	–	180	6
AMV	40	E-scan	~~173~~	~~5~~	~~487~~	~~45~~	–	–	–	–	~~645~~	~~60~~
AMV	40	E-scan	153	3	156	10	153	2.5	–	–	171	8
AMV	40	E-scan	149	3	164	12	–	–	–	–	182	10
AMV	40	E-scan	150	3	165	13	–	–	–	–	165	9
AMV	40	E-scan	149	3	170	14	–	–	–	–	186	11
AMV	40	E-scan	148	3	167	10	–	–	–	–	191	13
Weighted average			143	4	160	6	–	–			165	11
02123/AMV	40	B-scan	291	4	298	14	291	4	–	–	296	7
02123/AMV	40	E-scan	295	3	300	7	295	3	–	–	278	4
02123/NYP	20	E-scan	290	7	298	25	290	7	–	–	282	14
02123/NYP	20	B-scan	310	6	318	18	310	6	–	–	266	11
02123/GRM	40	B-scan	299	4	315	11	305	5	–	–	310	7
02123/GRM	20	B-scan	285	7	296	24	285	7	–	–	304	16
02123/GRM	40	E-scan	312	3	311	7	312	3	–	–	307	5
Weighted average			300	9	306	7	301	9			292	15

Values stroke with a dash are not included in the weighted average.

related to intra-run variation of laser homogeneity and to a variable response of zircon samples to the ablation process. Nevertheless, a direct link between elemental fractionation and zircon surface morphology, colour, age and U content has not been observed.

5.3. Age results on GRM zircons

Because TIMS data yield GRM zircon as discordant, ages from the different isotope ratios have been treated separately. However, for every single spot, concordance has been also tested.

All $^{206}Pb/^{238}U$ and $^{207}Pb/^{235}U$ determinations in B-scan mode at 40 μm of spot size yielded concordant ages whose weighted average (573 ± 4.4 Ma) is statistically equivalent to the TIMS age of 577 ± 8 (Table 5, Fig. 4). The $^{208}Pb/^{232}Th$ ages are slightly lower than concordant ages and the weighted average is 558 ± 9 Ma. The weighted average of $^{207}Pb/^{206}Pb$ ages is 565 ± 14 Ma. In this analytical run, standard reproducibility resulted to be to better than 2% for all isotope ratios and no common Pb was observed.

All $^{206}Pb/^{238}U$ and $^{207}Pb/^{235}U$ determinations but one yielded concordant ages with a weighted average of 583 ± 9 Ma (Table 5, Fig. 4). $^{208}Pb/^{232}Th$ and $^{207}Pb/^{206}Pb$ ages are 560 ± 17 and 560 ± 20 Ma, respectively. All age determinations are statistically in agreement with the TIMS value. Standard reproducibility in this analytical run is within 2.5% for all isotope ratios with the exception of the $^{208}Pb/^{232}Th$ (7.5% of variation). Also, in this run, no evidence of common Pb was observed.

The weighted $^{206}Pb/^{238}U$ and $^{207}Pb/^{235}U$ average ages at 40 μm of spot size in E-scan mode are 573 ± 9.8 and 573 ± 5.9 Ma, respectively (Table 5, Fig. 4). Contrarily to previous runs on the same sample, only two determinations yielded concordant ages. The $^{208}Pb/^{232}Th$ average age is 549 ± 8 Ma and that relative to $^{207}Pb/^{206}Pb$ ratio is 564 ± 24 Ma. The standard agreement in this run was to better than 1.9% for U/Pb ratios and 2.7% for $^{208}Pb/^{232}Th$ ratio. ^{204}Pb signal for all determination was within background level.

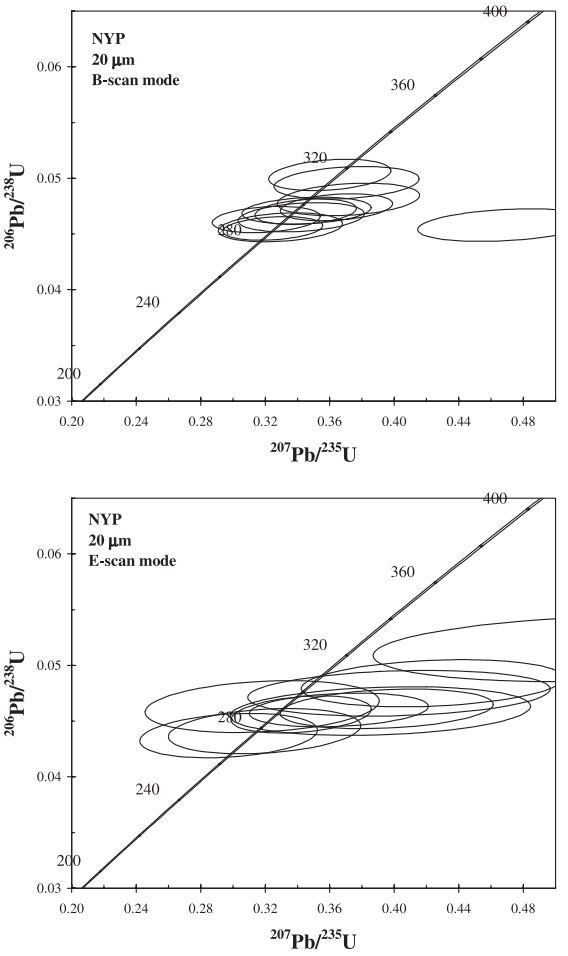

Fig. 5. Concordia diagrams for sample NYP.

5.4. Age results on NYP zircons

All $^{206}Pb/^{238}U$ and $^{207}Pb/^{235}U$ determinations but one yielded concordant ages and the weighted average (297 ± 7) is statistically in agreement with the TIMS value of 294 ± 1 Ma (Table 5, Fig. 5). Because of the low Pb* contents reliable $^{207}Pb/^{206}Pb$ ages were not achieved and also the $^{208}Pb/^{232}Th$ ages (256 ± 7 Ma) are not in agreement with the reference value. Standard agreement for this run was to better than 3% for U/Pb ratios and 3.7% for $^{208}Pb/^{232}Th$ ratio.

In E-scan mode, the weighted average of $^{206}Pb/^{238}U$ and $^{207}Pb/^{235}U$ ages is 289 ± 6.5 and 306 ± 24, respectively (Table 5, Fig. 5). Nearly half of the determinations yielded discordant ages and the weighted mean of concordant age is 287 ± 7 Ma. As with the analytical run carried out in B-scan mode, a significantly younger age was obtained for the $^{208}Pb/^{232}Th$ ratio (256 ± 7.4 Ma). In this run the agreement among standards resulted to be better than 2.4% for all isotope ratios.

5.5. Age results on AMV zircons

Three of the 11 $^{206}Pb/^{238}U$ and $^{207}Pb/^{235}U$ determinations result discordant and the mean weighted concordant age is 140 ± 2 Ma (Table 5, Fig. 6). No reliable ages were achieved on $^{207}Pb/^{206}Pb$ ratios for the very low Pb* content of this sample. The weighted

average age on the $^{208}Pb/^{232}Th$ ratio of 149 ± 8 Ma is statistically equivalent with the TIMS value. An agreement between the standards to better than 1.8% was achieved on the U/Pb ratios and of about 3.6% on the $^{208}Pb/^{232}Th$ ratio.

Data in E-scan mode (Table 5, Fig. 6) yielded weighted $^{206}Pb/^{238}U$ and $^{207}Pb/^{235}U$ average ages of 143 ± 4 and 160 ± 6 Ma, respectively, and only two determinations resulted concordant. The weighted $^{208}Pb/^{232}Th$ average age is 165 ± 11 Ma. One analysis revealed the presence of a significantly older core and it has been not considered. The intra-standard agreement is to better than 2.2% for all isotope ratios with the exception of the $^{207}Pb/^{235}U$ ratio (about 3.0%).

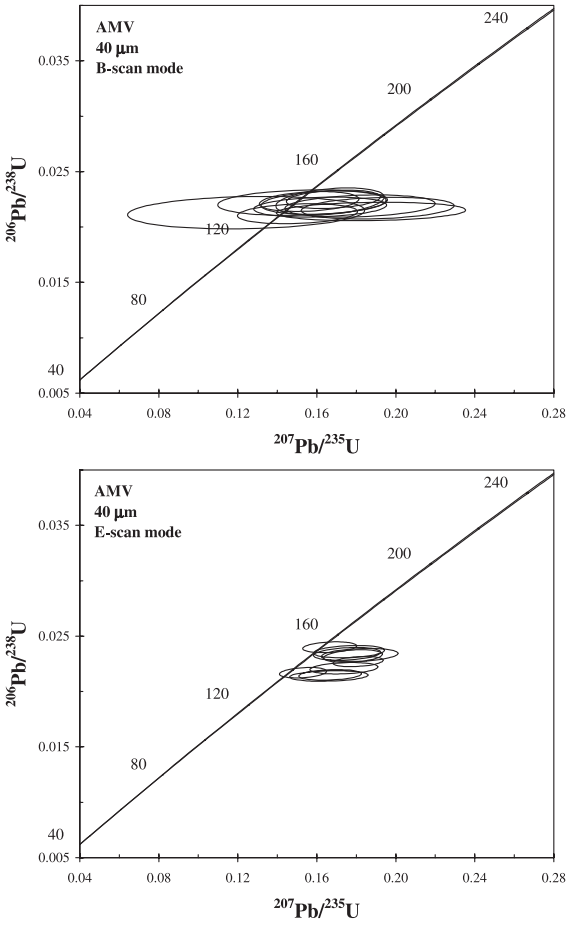

Fig. 6. Concordia diagrams for sample AMV.

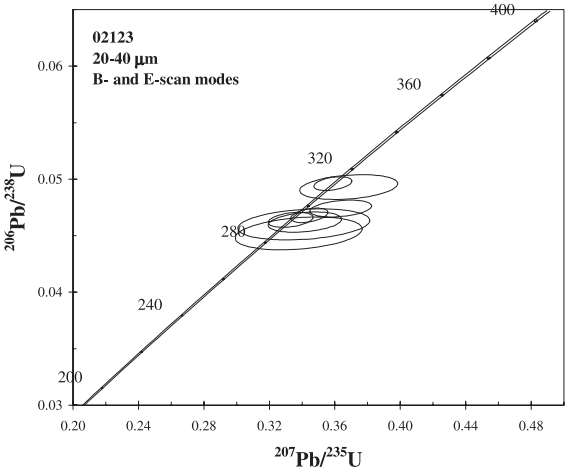

Fig. 7. Concordia diagram for sample 02123.

5.6. Age results on 02123 zircon

All determinations by LA–ICP–MS yielded concordant ages (Table 5, Fig. 7) in agreement with TIMS results. Nearly half of the concordant ages are statistically equivalent with the TIMS value of 295 ± 1 Ma (Ketchum et al., 2001) and only two determinations are significantly higher (310 ± 6 and 312 ± 3 Ma). Because age variation is not related to scan mode or spot size and a similar scattering was also observed in the LA–ICP–MS data from Ketchum et al. (2001), a slight microscale zoning of this zircon cannot be excluded. $^{208}Pb/^{232}Th$ ages span between 266 ± 11 and 310 ± 7 Ma.

6. Discussion

Internal precision (i.e., standard deviations of the mean of each individual analysis) and accuracy (i.e., the relative difference from reference values) are the two major parameters on which quality of data is established. In in situ Pb geochronology of zircons, the better is internal precision and accuracy, the higher is the possibility to distinguish, within a single grain, between different geological events. Because age determination is the final aim of this technique, in the following sections, internal precision and accuracy on the ages will be discussed. We must consider however that internal precision on the age represents

the propagation of the error associated to isotope ratios through age calculation.

Zircon samples considered in the present work and the different conditions at which analytical runs were carried out allow to investigate the influence of spatial resolution, Pb* and scan mode on internal precision and accuracy. Within a single analytical run, internal precision on the age determination is relatively constant and a mean precision value (calculated as the average of the 2σ error in percent on the ages) has thus been considered for each run. As it concerns accuracy, it must be considered that it is calculated by comparing microanalytical and bulk results and that the correspondence of these values is often hampered by several factors (e.g., zircon homogeneity, presence of microfractures not detected during the analysis). However, in order to make age results as much comparable as possible with TIMS, data accuracy has been evaluated on the weighted mean of all replicates.

6.1. Spatial resolution

Spatial resolution rules the amount of analyte sent to the mass spectrometer. The smaller is spot size, the lower is instrumental sensitivity and, as previously shown, the higher is U/Pb laser induced elemental fractionation.

The direct influence of spatial resolution on internal precision and accuracy can be evaluated on the two runs carried out in B-scan mode at 20 and 40 μm of spot size on GRM zircons. The mean internal precision at 40 μm of spot size is about 1.0% on the $^{206}Pb/^{238}U$ age and about 1.7% on $^{207}Pb/^{235}U$ age. A value of about 8.1% and 1.3% was achieved on the $^{207}Pb/^{206}Pb$ and $^{208}Pb/^{232}Th$ ages, respectively. Accuracy at 40 μm of spot size on the concordant age is about 0.7%. If apparent ages from single $^{206}Pb/^{238}U$ and $^{207}Pb/^{235}U$ isotope ratios are considered, accuracy is between 1.0% and 1.6%. On $^{207}Pb/^{206}Pb$ and $^{208}Pb/^{232}Th$ ages accuracy is 2.4% and 3.6 %, respectively. By reducing the spot size from 40 to 20 μm, average signal intensity decrease of about 40% and internal precision decreases of about 1.5 times for all ages. $^{206}Pb/^{238}U$ age is affected by an error of about 1.6% and that relative to the $^{207}Pb/^{235}U$ ratio by an error of about 2.6%. The same response of internal precision as a function of spot size was observed also on sample 02123. No significant changes in accuracy (about 1.0%) on concordant age were observed by reducing spot size. However, accuracy on single isotope ratios is about two times lower. A slightly lower accuracy (about 3.3%) was also achieved on the $^{207}Pb/^{206}Pb$ age.

These results indicate that geologically meaningful ages on relatively Pb*-rich zircons can be achieved also with a spatial resolution down to 20 μm that well compare with that commonly used by ion microprobe techniques.

6.2. Radiogenic Pb content

Due to the very small amounts of sampled material by microanalytical techniques relative to bulk analyses (e.g., TIMS), Pb* content in zircon and in particular that of ^{207}Pb is a critical parameter affecting in terms of precision and accuracy the possibility to achieve meaningful geological ages. Pb* content in zircons is a function of crystal age and initial U content. In order to investigate the minimum and geologically acceptable detectable age with our instrument, variation of precision and accuracy as a function of Pb* in zircon have been calculated.

In Fig. 8, the variation of internal precision (2σ) as a function of the Pb* content in zircon in B-scan mode at constant spot size (40 μm; filled symbols) on the $^{206}Pb/^{238}U$, $^{207}Pb/^{235}U$ and $^{208}Pb/^{232}Th$ ages is reported. Internal precision on the three apparent ages decreases with the increasing of the Pb* content in zircon. Precision on the $^{206}Pb/^{238}U$ age is about 1.0% at 40 ppm of Pb* (zircon GRM), 1.3% at 8 ppm of Pb* (zircon 02123) and up to 3.8% at 0.7 ppm of Pb* (zircon AMV). Internal precision on the $^{207}Pb/^{235}U$ age is more sensitive to the decrease in Pb* content. At 40 ppm of Pb* in zircon, internal precision on the $^{207}Pb/^{235}U$ age is about 1.7 times higher than on $^{206}Pb/^{238}U$ age, at 10 ppm of Pb* about 3 times higher and at 0.7 ppm of Pb* up to 4.6 times higher. A similar dependence of internal precision from Pb* in zircon has been also observed for the $^{208}Pb/^{232}Th$ age.

As well as internal precision, at constant conditions of scan mode and spot size, also accuracy shows a clear inverse relationship with Pb* content in zircon (Fig. 9). Accuracy on concordant and $^{207}Pb/^{235}U$ ages ranges from about 1% at 40 ppm of Pb* up to about

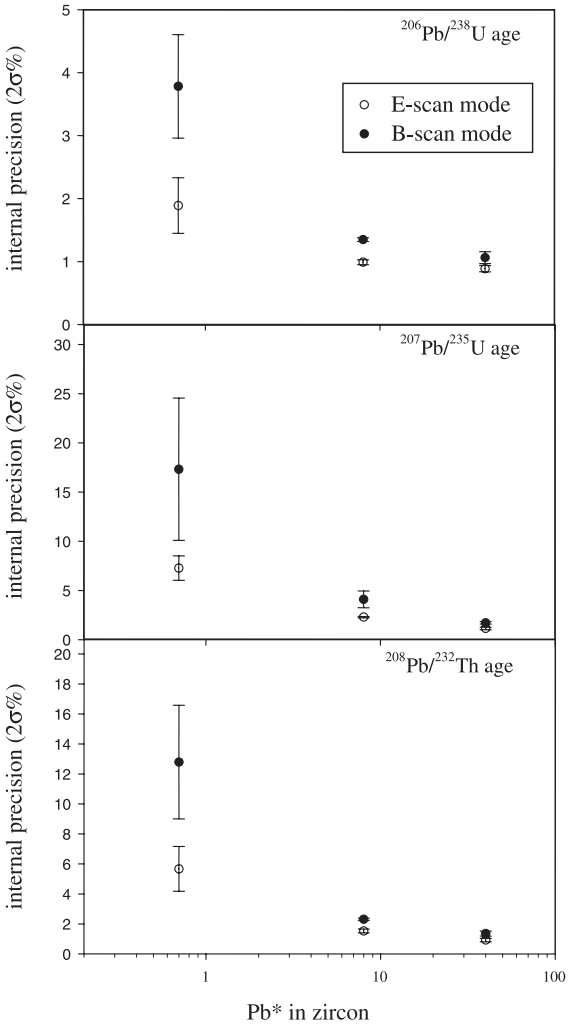

Fig. 8. Internal precision variation on $^{206}Pb/^{238}U$, $^{207}Pb/^{235}U$ and $^{208}Pb/^{232}Th$ as a function of radiogenic Pb in zircon.

5% for zircons with less than 1 ppm of Pb*. Accuracy on $^{206}Pb/^{238}U$ age does not significantly change between 40 and 8 ppm of Pb* in zircon. However, significantly higher values (about 4.8%) are observed for the most Pb* depleted zircon. Noticeably, accuracy does not show any clear relationship with residual error stemming from U/Pb laser induced elemental fractionation. Most likely, it is not thus the main source of error.

Despite a significantly lower internal precision, geologically meaningful ages can be achieved down to less than 1 ppm of radiogenic Pb content in zircon. This indicates that zircons even younger than 150 Ma can be dated if higher initial U contents than those of the selected sample are present or if the only $^{206}Pb/^{238}U$ ratio is considered.

6.3. Scan mode

The influence of scan mode on precision and accuracy is mainly related to (i) the different acquisition efficiency (93% in E-scan vs. 63% in B-scan), (ii) the different number of sweeps (i.e., 820 in E-scan mode vs. 410 in B-scan) and (iii) the different sensitivity (i.e., in E-scan mode sensitivity on ^{238}U is about 45% lower than in B-scan mode) allowed by the two acquisitions lists.

The analytical run carried out in E-scan mode at 40 μm of spot size on zircon GRM (40 ppm of Pb*) gives significantly better results in terms of

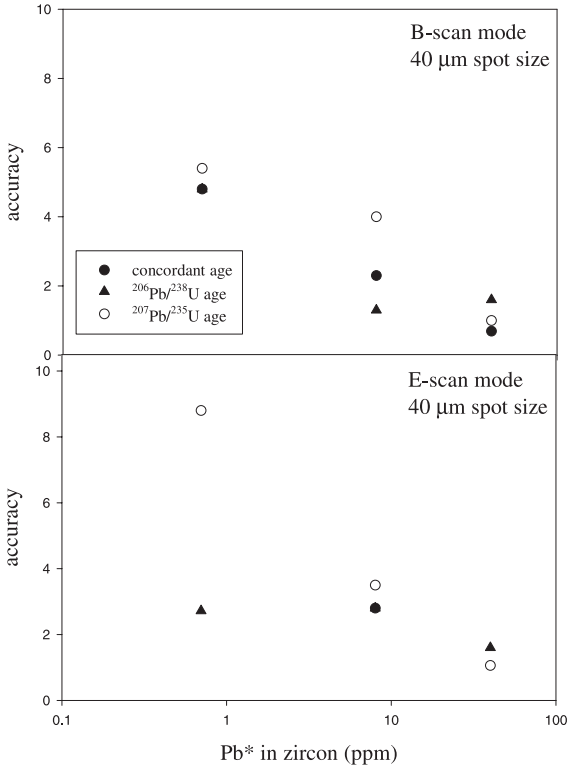

Fig. 9. Accuracy variation as a function of radiogenic Pb content in zircon.

internal precision than that in B-scan mode. The error associated with the $^{206}Pb/^{238}U$ age is 0.89%, that with the $^{207}Pb/^{235}U$ age is 1.1% and that with $^{208}Pb/^{232}Th$ ages is 0.92%. These values are up to 35% lower than those carried out in B-scan mode on the same zircon. As shown in Fig. 8, with the decreasing of the Pb* content in zircon there is an increase of internal precision from the E-scan (open symbols) if compared to B-scan (filled symbols). If the zircon AMV is considered (0.7 ppm of Pb*), internal precision in E-scan mode on $^{206}Pb/^{238}U$, $^{207}Pb/^{235}U$ and $^{208}Pb/^{232}Th$ ages is more than two times better than in B-scan mode. Data also reveal that, especially on zircon with low Pb* contents, the E-scan mode allows a higher reproducibility of internal precision. Contrasting results were achieved in the analytical runs at 20 μm of spot size. On both NYP and 02123 zircons, internal precision in E-scan mode is up to 40% lower than that in B-scan mode. These contrasting results are due to the loss in sensitivity proportional to the difference from the nominal magnet mass, induced by the E-scan mode, estimated up to 45% for ^{232}Th and ^{238}U masses. At 40 μm of spot size, despite the loss in sensitivity that is partly compensated by the increased acquisition efficiency, signals are still very high (e.g., about $1.5e^6$ cps of ^{238}U on zircon 91500) and, in E-scan mode, the more dense sampling of the transient signal, resulting from the higher number of sweeps, allows a significant gain in the internal precision of the isotope ratio relative to B-scan. At 20 μm of spot size, signals are about two times lower than at 40 μm, due to the lower amount of ablated material and a further 40% of signal, related to E-scan mode, has to be subtracted. The result is a sensitivity about one order of magnitude lower. If mass ^{235}U is considered, signal on zircon 91500 at 40 μm in B-scan mode is about 12,000 and about 1100 cps at 20 μm of spot size in E-scan mode. On masses with low abundance (e.g., ^{235}U and ^{207}Pb) the lower sensitivity has thus a greater effect on internal precision relative to the gain produced by the more dense sampling of the signal of the E-scan mode.

If weighted average ages from the single isotope ratios are considered, age determinations in E-scan mode are statistically equivalent to those determined in B-scan mode (see Table 5). In particular, as shown in Fig. 9, accuracy on GRM zircon in E-scan mode is equivalent to that in B-scan mode for both $^{206}Pb/^{238}U$ and $^{207}Pb/^{235}U$ ages. With the decreasing of Pb* in zircon the E-scan mode furnish a lower accuracy on the $^{207}Pb/^{235}U$ ages because of the loss in sensitivity. However, a slightly better accuracy on the $^{206}Pb/^{238}U$ ages is achieved on young zircon. The analyses carried out in E-scan mode on GRM, NYP and AMV zircons furnish a higher number of discordant ages relative to those in B-scan mode. This difference is most likely related to the higher precision of the E-scan mode that better highlight even small degree of discordance (TIMS determinations yielded discordant ages for all these zircons). A low internal precision may false zircon concordance. A poorer Pb/U ratio measurement in E-scan than in B-scan is also ruled out by the fact that concordant ages were obtained in both modes on the concordant 02123 zircon with comparable accuracy.

6.4. Comparison with literature data

Most of the age determinations carried out with other LA–ICP–MS instruments have been carried out on Proterozoic zircons, thus a direct comparison with the results of the present work is not straightforward. A realistic comparison should be based on the same samples or on samples with the same age and the same U content.

Zircons with ages comparable to those of the present work have been analysed by Li et al. (2001) and Horn et al. (2000). Li et al. (2001) used a quadrupole instrument coupled with 266 nm Nd:YAG lasers adopting the method of the linear ablation. $^{206}Pb/^{238}U$ ages show a precision on the weighted average of about 2–5% and up to 6–10%, if internal precision on each single ages is considered. Data obtained in the present work on the same ratio, even considering those performed at 20 μm of spot size, are at least two times more precise. Precision on $^{206}Pb/^{238}U$ and $^{206}Pb/^{207}Pb$ ages obtained in this work on zircon GRM is comparable to that obtained by Horn et al. (2000) on the ANU Shrimp zircon standard SL-13 (572 ± 0.4 Ma; Claoué-Long et al., 1995) with a quadrupole-based ICP–MS and with a highly homogeneous 193-nm excimer laser.

7. Conclusions

The Pb geochronological capabilities of a LA–ICP–MS instrument based on the coupling of a single-collector sector-field mass spectrometer and a 213-nm laser source have been tested on a series of not-standard zircons ranging in age between 150 and 577 Ma. In order to evaluate the instrumental limitations of this technique, internal precision and accuracy variations have been monitored as a function of spatial resolution, Pb* content of zircon and mass spectrometer scan options.

Results indicate that:

(1) Geologically meaningful ages on the three independently determined $^{206}Pb/^{238}U$, $^{207}Pb/^{235}U$ and $^{208}Pb/^{232}Th$ ratios can be achieved by this LA–ICP–MS instrument down to 1 ppm of Pb* in zircon. Reliable $^{207}Pb/^{206}Pb$ ages can be achieved only in zircon with about 40 ppm of Pb*.
(2) At a spatial resolution of 40 μm the electrostatic scan mode of mass spectrum is more suitable and gives internal precision values (2σ) on $^{206}Pb/^{238}U$, $^{207}Pb/^{235}U$ and $^{208}Pb/^{232}Th$ ages to better than 1.1% on zircons with about 40 ppm of Pb*. On young zircons (Pb* <1 ppm), internal precision values to better than 7% ($^{207}Pb/^{235}U$ age) have been achieved.
(3) A spatial resolution of 20 μm can be adopted on relatively Pb*-rich zircons even if internal precision is about 1.5 times lower than at 40 μm of spot size. On young and Pb* depleted zircons (<10 ppm), the magnetic scan mode is preferable because of the higher sensitivity on high masses relative to E-scan mode.
(4) Accuracy is not significantly sensitive to scan mode and is rather influenced by Pb* content of zircon, with values ranging between 1% and 5%.

Acknowledgements

I am indebted to Piero Bottazzi for the many theoretical and practical advices he gave me. Jean-Louis Paquette kindly provided zircon samples and the reference ages, determined by TIMS. Riccardo Vannucci is thanked for the constructive suggestions and M. Palenzona for the technical assistance at the LA–ICP–MS instrument. The paper has benefited from constructive reviews of I. Horn and T. Hirata. Support for this work was provided by Consiglio Nazionale delle Ricerche-Agenzia 2000 (project "Sviluppo di datazioni U/Pb di zirconi mediante Laser Ablation Microprobe–Inductively Coupled Plasma–Mass Spectrometry: prime applicazioni alla geocronologia di eventi magmatici connessi all'orogenesi Alpina") to Massimo Tiepolo. The P.N.R.A. has supported the purchase of the laser probe and of the mass spectrometer. **[RR]**

References

Claoué-Long, J.C., Compston, W., Roberts, J., Fanning, C.M., 1995. Two caboniferous ages: a comparison of SHRIMP zircon dating with conventional zircon ages and $^{40}Ar/^{39}Ar$ analysis. Geochronology Time Scales and Global Stratigraphic correlation. SEPM Special Publication, pp. 3–21.

Eggins, S.M., Kinsley, L.P.J., Shelley, J.M.M., 1998. Deposition and elemental fractionation processes during atmospheric pressure laser sampling for analysis by ICPMS. Appl. Surf. Sci. 127, 278–286.

Feng, R., Machado, N., Ludden, J., 1993. Lead geochronology of zircon by laserprobe–inductively coupled plasma mass spectrometry (LP–ICP–MS). Geochim. Cosmochim. Acta 57, 3479–3486.

Fryer, B.J., Jackson, S., Longerich, H., 1993. The application of laser ablation microprobe–inductively coupled plasma–mass spectrometry (LAM–ICP–MS) to in situ (U)–Pb geochronology. Chem. Geol. 109, 1–8.

Hirata, T., 1997. Soft ablation technique for laser ablation–inductively coupled plasma mass spectrometry. J. Anal. At. Spectrom. 12, 1337–1342.

Hirata, T., 2002. Chemically assisted-laser ablation–ICP–mass spectrometry. 12th Annual Goldschmidt Conference, Davos Switzerland, August 18–23, 2002. Abstracts volume, A331.

Hirata, T., Nesbitt, R.W., 1995. U–Pb geochronology of zircon: evaluation of the laser probe–inductively couplet plasma–mass spectrometry technique. Geochim. Cosmochim. Acta 59, 2491–2500.

Horn, I., Rudnick, R., McDonough, F., 2000. Precise elemental and isotope ratio determination by simultaneous solution nebulization and laser ablation–ICP–MS: application to U–Pb geochronology. Chem. Geol. 164, 281–301.

Horstwood, M.S.A., Foster, G.L., Parrish, R.R., Noble, S.R., 2001. Common-Pb and inter-element corrected U–Pb geochronology by LA–MC–ICP–MS. 11th Annual Goldschmidt Conference. Abstract 3698.

Jackson, S.E., 2001. The application of Nd:YAG lasers in LA–ICP–MS. In: Sylvester, P. (Ed.), Laser-Ablation–ICPMS in the Earth Sciences Principles and Applications. Short

Course Series, vol. 29. Mineralogical Association of Canada, St. John's Newfoundland, pp. 29–47.

Jackson, S.E., Günther, D., 2002. Studies of the source of laser induced isotopic bias in LA–ICP–MC–MS. 12th Annual Goldschmidt Conference, Davos Switzerland, August 18–23, 2002. Abstracts volume, A359.

Jackson, S.E., Longerich, H., Dunning, G.R., Fryer, B.J., 1992. The application of laser-ablation microprobe–inductively coupled plasma–mass spectrometry (LAM–ICP–MS) to in situ trace element determinations in minerals. Can. Mineral. 30, 1049–1064.

Jackson, S.E., Horn, I., Longerich, H., Dunning, G.R., 1996. The application of laser ablation microprobe (LAM)–ICP–MS to in situ U–Pb zircon geochronology. In: Goldschimdt, V.M. (Ed.), Conf. J. Conf. Abstracts, vol. 1, pp. 283.

Jackson, S.E., Pearson, N.J., Griffin, W.L., 2001. In situ isotope ratio determination using laser-ablation (LA)–magnetic sector–ICP–MS. In: Sylvester, P. (Ed.), Short Course Series, vol. 29. Mineralogical Association of Canada, St. John's Newfoundland, pp. 105–119.

Jeffries, T.E., Jackson, S.E., Longerich, H.P., 1998. Application of a frequency quintupled Nd:YAG source ($\lambda = 213$ nm) for laser ablation ICP–MS analysis of minerals. J. Anal. At. Spectrom. 13, 935–940.

Ketchum, J.W.F, Jackson, S.E., Culshaw, N.G., Barr, S.M., 2001. Depositional and tectonic setting of the Paleoproterozoic Lower Aillik Group, Makkovik Province, Canada: evolution of a passive margin–foredeep sequence based on petrochemistry and U–Pb (TIMS and LAM–ICP–MS) geochronology. Precambrian Res. 105, 331–356.

Guillong, M., Günther, D., 2002. Effect of particle size distribution on ICP–induced elemental fractionation in laser ablation–inductively coupled plasma–mass spectrometry. J. Anal. At. Spectrom. 17, 831–837.

Guillong, M., Horn, I., Günther, D., 2002. Capabilities of a homogenized 266 nm Nd:YAG laser ablation system for LA–ICP–MS. J. Anal. At. Spectrom. 17, 8–14.

Günther, D., Heinrich, C.A., 1999. Comparison of the ablation behavior of 266 nm Nd:YAG and 193 nm ArF excimer lasers for LA–ICP–MS analysis. J. Anal. At. Spectrom. 14, 1369–1374.

Günther, D., Hattendorf, B., 2001. Elemental fractionation in LA–ICP–MS. In: Sylvester, P. (Ed.), Laser-Ablation–ICPMS in the Earth Sciences Principles and Applications. Short Course Series, vol. 29. Mineralogical Association of Canada, St. John's Newfoundland, pp. 83–93.

Latkoczy, C., Günther, D., 2002. Enhanced sensitivity in inductively coupled plasma sector field mass spectrometry for direct solid analysis using laser ablation (LA–ICP–SFMS). J. Anal. At. Spectrom. 17, 1–8.

Li, X.-H., Liang, X., Sun, M., Liu, Y., Tu, X., 2000. Geochronology and geochemistry of single-grain zircons: simultaneous in-situ analysis of U–Pb age and trace elements by LAM–ICP–MS. Eur. J. Mineral. 12, 1015–1024.

Li, X.-H., Liang, X., Sun, M., Guan, H., Malpas, J.G., 2001. Precise $^{206}Pb/^{238}U$ age determination on zircons by laser ablation microprobe–inductively coupled plasma–mass spectrometry using continuous linear ablation. Chem. Geol. 175, 209–219.

Longerich, E., Günther, D., Jackson, S.E., 1996. Elemental fractionation in laser ablation inductively coupled plasma mass spectrometry. Fresenius J. Anal. Chem. 355, 538–542.

Ludwig, K.R., 2000. Isoplot—a geochronological toolkit for Microsoft Excel. Berkeley Geochronology Center, Special Publication, vol. 1a, p. 53.

Machado, N., Simonetti, A., 2001. U–Pb dating and Hf isotopic composition of zircon by laser-ablation–MC–ICP–MS. In: Sylvester, P. (Ed.), Laser-Ablation–ICPMS in the Earth Sciences Principles and Applications. Short Course Series, vol. 29. Mineralogical Association of Canada, St. John's Newfoundland, pp. 121–147.

Mank, A.J.G., Mason, P., 1999. A critical assessment of laser ablation ICP–MS as an analytical tool for depth analysis in silica-based glass samples. J. Anal. At. Spectrom. 14, 1143–1153.

Paquette, J.-L., Nédélec, A., Moine, B., Rakotondrazafy, M., 1994. U–Pb, single zircon evaporation, and Sm–Nd isotopic study of a granulite domain in SE Madagascar. J. Geol. 102, 523–538.

Seyler, M., Paquette, J.-L., Ceuleneer, G., Kienast, J.-R., Loubet, M., 1998. Magmatic underplating, metamorphic evolution and ductile shearing in a Mesozoic lower crustal-upper mantle unit (Tinaquillo, Venezuela) of the Caribbean belt. J. Geol. 106, 35–58.

Tiepolo, M., Bottazzi, P., Palenzona, M., Vannucci, R., 2003. A laser probe coupled with ICP–double-focusing sector-field mass spectrometer for in situ analysis of geological samples and U–Pb dating of zircon. Can. Mineral. (in press).

Wiedenbeck, M., Alle, P., Corfu, F., Griffin, W.L., Meier, M., Oberli, F., Von Quadt, A., Roddick, J.C., Spiegel, W., 1995. Three natural zircon standards for U–Th–Pb, Lu–Hf, trace elements ad REE analyses. Geostand. Newsl. 19, 1–23.

Williams, I.S., 1998. U–Th–Pb geochronology by ion microprobe. In: McKibben, M.A., Shanks, W.C., Ridley, W.I. (Eds.), Application of Microanalytical Techniques to Understanding Mineralizing Processes. Reviews in Economic Geology, vol. 7, pp. 1–35.